Advanced Composites and Hybrid Materials (2023) 6:91
https://doi.org/10.1007/s42114-023-00669-6

RESEARCH

Hierarchical porous Mo-Co_3O_4-CNTc nanosheets for aqueous rechargeable zinc ion batteries with ultralong life

Changwei Lai[1,2] · Xiaoxiao Qu[3] · Yao Guo[1] · Miaomiao Li[1] · Haixiang Song[1] · Kwan Lee[2,4]

Received: 5 November 2022 / Revised: 29 March 2023 / Accepted: 8 April 2023 / Published online: 21 April 2023
© The Author(s), under exclusive licence to Springer Nature Switzerland AG 2023

Abstract

Aqueous rechargeable zinc ion batteries (ZIBs) are a promising next-generation energy storage device, which suffers from poor capacity and limited cycle life. In this work, a ZIB cathode material was reported, consisting of a composite of Co_3O_4 doped with Mo and carboxylic carbon nanotubes (Mo-Co_3O_4-CNTc), with a hierarchical porous structure arising from ultrathin nanosheets. The composite was prepared via a sol-gel method in an emulsion system. The experimental electrochemical data and density-functional first-principles calculations showed that the as-prepared Mo-Co_3O_4-CNTc composites with 152.9 mAh g^{-1} showed superior electrochemical performance compared to pure Co_3O_4 (as 107.3 mAh g^{-1}) and Mo-Co_3O_4 (as 112.0 mAh g^{-1}) electrode materials. Furthermore, the as-prepared MoCo-Zn batteries, with zinc metal foil anode and Mo-Co_3O_4-CNTc cathode, exhibited a specific capacity of 195.7 mAh g^{-1} at 0.5 A g^{-1}, energy density of 237.6 Wh kg^{-1} at 1692.4 W kg^{-1}, and a remarkable ultralong cycling life of over 10,000 cycles with 85.1% capacity retention. The superior performance can be attributed to the hierarchical porous structures with open spaces acting as "ion-buffering reservoirs." The summary of zinc ion storage mechanism in the MoCo-Zn batteries was investigated during the charge-discharge process. Therefore, this work promotes the development of innovative strategies to synthesize carbon-modified composites with hierarchical porous nanosheets as cathode materials, for the ultra-long cycle-life aqueous rechargeable ZIBs.

Keywords Mo-Co_3O_4-CNTc composites · Zinc ion batteries · Ultralong life · Zinc ions storage mechanism · First-principles calculations

1 Introduction

With the growing energy crisis and population explosion, clean alternative energy storage systems remain a significant challenge to attaining carbon neutrality and environmental protection [1–5]. Next-generation energy storage devices, such as aqueous rechargeable batteries [6], lithium ion batteries [7–9], lithium-oxygen batteries [10, 11], and supercapacitors [12–17], have attracted significant research interest. Aqueous rechargeable zinc ion batteries (ZIBs) are a promising technology due to their environmental friendliness, intrinsic safety, low cost, high specific capacity, and high energy density [18]; however, they show restricted capacity and limited cycle life [19, 20]. Currently, ZIB performance is mainly limited by cathode materials, which need to be further developed to achieve stable cycle life and suitable crystalline structures [21].

Among cathode materials, Co_3O_4 displays low cost, excellent stability, high theoretical capacity, and excellent electrochemical performance; however, it suffers from low

✉ Changwei Lai
laichangwei0229@163.com

✉ Haixiang Song
13837213690@163.com

✉ Kwan Lee
kwanlee@ks.ac.kr; kwanlee@suwon.ac.kr

[1] Henan Joint International Research Laboratory of Nanocomposite Sensing Materials, School of Materials Science and Engineering, Anyang Institute of Technology, Anyang 455000, People's Republic of China

[2] Department of Advanced Materials Engineering, Kyungsung University, Busan 48434, Republic of Korea

[3] Department of Optics and Mechatronics Engineering, College of Nanoscience and Nanotechnology, Pusan National University, Busan 46241, Republic of Korea

[4] Department of Electronic Materials Engineering, The University of Suwon, Hwaseong 18323, Republic of Korea

practical capacity due to its intrinsic electronic conductivity [7, 22–29]. The electronic transport in Co_3O_4 has been improved by two strategies, i.e., by doping ions and by incorporating carbon-based materials as "express channels" [30–38]. Compared with monometallic oxides, binary metal oxides possess a more complicated chemical composition and show a decreased band gap; all these factors act synergistically and improve electronic conductivity and electrochemical performance [39, 40]. For instance, Mo-doped Co_3O_4 electrodes exhibit superior electrochemical performance due to the synergy between the $Co^{2+}/Co^{3+}/Co^{4+}$ and Mo^{6+}/Mo^{4+} redox couples during the electrochemical processes [41]. Hence, designing promising Mo-doped Co_3O_4 cathode materials with high electrochemical performance can help achieve high specific capacity and long cycling performance of MoCo-Zn batteries.

Herein, we report the fabrication of hierarchical porous Mo-Co_3O_4-CNTc composites as cathode materials for aqueous rechargeable ZIBs. The construction process of Mo-Co_3O_4-CNTc composites involves the oil-in-water (O/W) emulsion system, which is a facile method and involves industrial manufacturing equipment. A series of interconnected CNTs act as "express channels" and are connected to the Mo-Co_3O_4 nanosheets by a sol-gel method, leading to 3D conductive networks with improved electronic conductivity. The obtained Mo-Co_3O_4-CNTc cathode material exhibited a specific capacity of 152.9 mAh g^{-1} at 0.5 A g^{-1}, and showed excellent cycling performance, with a 80.3% capacity retention even after 4000 charge-discharge cycles at 25 A g^{-1}. Notably, the assembled MoCo-Zn batteries also exhibited excellent electrochemical performance. Additionally, the Zn^{2+} ion storage mechanism of the Mo-Co_3O_4-CNTc cathode was further investigated via ex situ XRD patterns, Raman spectra, and XPS measurements to characterize structural evolution at certain voltages to further investigate MoCo-Zn batteries.

2 Experimental section

2.1 Materials

All reagents used in this work are of analytical grade. $Co(NO_3)_2{\cdot}6H_2O$ (> 98.5%), $Na_2MoO_4{\cdot}2H_2O$ (> 99.0%), CH_2Cl_2, polyethylene glycol (PEG, molecular weight 6000), ammonia water (25~28%), KOH (> 85.0%), acetylene black, polyvinylidene difluoride (PVDF), and *N*-methyl-2-pyrrolidone (NMP, 99.5%) were purchased from Sinopharm Chemical Reagent Co., Ltd. The carboxylic CNT (CNTc) was bought from Nanjing/Jiangsu XFNANO Materials Tech Co., Ltd.

2.2 Preparation of hierarchical porous Mo-Co_3O_4-CNTc composites

The hierarchical porous Mo-Co_3O_4-CNTc composites were synthesized in an O/W emulsion system by a sol-gel method. The polyethylene glycol (PEG, 6 g, molecular weight 6000) was dissolved in dichloromethane (CH_2Cl_2, 30 mL), and the CNTc (acid-modified CNT, 0.12 g) was dispersed in water (130 mL) under sonication. Then, PEG/CH_2Cl_2 was added to CNTc/water under high magnetic stirring. $Co(NO_3)_2{\cdot}6H_2O$ (0.582 g, 2 mmol) and $Na_2MoO_4{\cdot}2H_2O$ (0.0484 g, 0.2 mmol) were dissolved in water (20 mL), and then added to the mixture dropwise. With the volatilization atmosphere of 8 mL of ammonia water, the system of the emulsion was covered in a beaker and further reacted for 12 h to obtain the Mo-$Co(OH)_x$-CNTc composites as precursors. Then, the precipitates were ultrasonically washed and dried at 60 °C in a vacuum oven. Finally, the Mo-Co_3O_4-CNTc composites were obtained by an annealing process at 250 °C in a muffle furnace for 2 h. Moreover, a series of Mo-Co_3O_4 electrode materials were further prepared with different Mo-Co molar ratios of 1:10, 5:10, and 10:10 for comparison with pure Co_3O_4 and Mo-Co_3O_4-CNTc composites.

2.3 Material characterization

The Mo-Co_3O_4-CNTc composites were characterized by X-ray diffraction (XRD, Bruker, Germany), thermogravimetric analysis (TGA, SDT-Q600), X-ray photoelectron spectroscopy (XPS, ESCALAB-250), scanning electron microscopy (SEM, HITACHI S-4800), transmission electron microscopy (TEM, Philips Tecnai-12), high-resolution TEM (HRTEM), and Raman spectroscopy (LabRAM HR Evolution). The surface areas and pore volume were confirmed by the Brunauer–Emmett–Teller (BET) and Barrett–Joyner–Halenda (BJH) methods (BSD-660 equipment), respectively.

2.4 Assembly of zinc ion batteries

The MoCo-Zn ZIBs were fabricated with a Zn metal foil as anode and 1 mg of hierarchically porous Mo-Co_3O_4-CNTc composite as cathode, deposited on a Ni foam current collector (1 × 1 cm^2), and 6 M KOH with 0.2 M zinc acetate as electrolyte. The MoCo-Zn batteries were prepared based on a nickel foam (4 × 4 cm^2) current collector, with a loading of 16 mg of Mo-Co_3O_4-CNTc and Zn metal foil in a soft package of polyethylene (PE).

2.5 Electrochemical characterization

The electrochemical properties of Mo-Co_3O_4-CNTc (with Hg/HgO as reference electrode) and MoCo-Zn batteries were

characterized by cyclic voltammetry (CV), galvanostatic charge-discharge (GCD), and electrochemical impedance spectroscopy (EIS), with an electrochemical workstation (CHI660e and SLAN-CT2001A). The specific capacities of the Mo-Co_3O_4-CNTc electrodes and MoCo-Zn batteries were obtained according to the following equation:

$$C^* = It/3.6m \tag{1}$$

wherein C^*, I, t, and m refer to the capacity (mAh g^{-1}), discharge current (A), discharging time (s), and the mass of active mass on working electrode (g), respectively. Furthermore, the energy density (E, W h kg^{-1}) and power density (P, W kg^{-1}) were calculated according to equations:

$$E = \int IVdt/m \tag{2}$$

$$P = E/t \tag{3}$$

wherein V is the discharging voltage (V).

2.6 Computational methods

All first-principles calculations were conducted using density functional theory (DFT) as implemented in the Vienna ab initio simulation package (VASP) [42, 43] code interfaced with the MedeA software. The frozen-core projector augmented wave (PAW) [44] technique of Blöchl was employed to represent the inner core potentials. The generalized gradient approximation, as described by Perdew-Burke-Ernzerhof (GGA-PBE) [45], was adopted to treat the exchange-correlation energy. The kinetic energy cutoff of 400 eV and Gaussian smearing [46] of 0.1 eV were set for all calculations. The sampling of the Brillouin zone was obtained from the Monkhorst-Pack [47] k-point grid, with a resolution of 0.2 $Å^{-1}$. A vacuum layer of about 15 Å was used to avoid interactions between the adjacent layers. Spurious slab-to-slab dipole interactions were also corrected (IDIPOL = 3). The van der Waals (vdW) effects were described using a dispersion-corrected DFT-D3 scheme [48] with Becke-Johnson damping. Hubbard correction [49], with U_{eff} = 4 eV for Co and U_{eff} = 1 eV for Mo, was selected to describe the strong correlation effect. Geometries were fully optimized until the energy converged to 1.0×10^{-6} and the force converged to 0.005 eV/Å.

3 Results and discussion

The synthesis process to obtain hierarchical porous Mo-Co_3O_4-CNTc composites is schematically depicted in Fig. 1a. The Mo-$Co(OH)_x$-CNTc composites, as precursors, were prepared in the O/W emulsion. Remarkably, the Mo-Co_3O_4-CNTc composites can be obtained in the annealing process, in which the CNTc content was confirmed to be about 21.8% from TGA curves (Fig. S1). The crystal structure of the Mo-Co_3O_4-CNTc composites was confirmed to be the cubic phase (JCPDS no. 42-1467) by the XRD patterns (Fig. 1b), which shows diffraction peaks for the (111), (220), (311), (222), (400), (422), (511), and (440) planes. Furthermore, the chemical composition and state were determined via XPS (Fig. S2a). The Co 2p spectra (with shake-up satellites ("Sat.") at 787.6 and 804.2 eV) were detected for Co^{3+} and Co^{2+} (Fig. 1c), thus indicating that the fitting peaks at band energy of 780.5 and 795.5 eV can be assigned to Co^{3+}, and the fitting peaks at 782.0 and 797.0 eV can be ascribed to Co^{2+} [50, 51]. The Mo 3d spectrum (Fig. 1d) can be assigned to Mo $3d_{3/2}$ at 235.3 eV and Mo $3d_{5/2}$ at 232.2 eV, thus indicating the existence of Mo^{6+} with a width of 3.1 eV in the Mo-Co_3O_4-CNTc composites [32, 52]. Furthermore, the spectrum of O1s can be resolved as the lattice oxide ions O^{2-} at 530.3 eV, defective oxide ions O^{x-} at 531.5 eV, and adsorbed surface water at 533.5 eV in Fig. 1e. The two peaks at 284.8 and 286.2 eV can be attributed to C–C/C = C and C–O–C, respectively (Fig. S2b), thus confirming the successful preparation of the Mo-Co_3O_4-CNTc composites.

The detailed morphologies of the obtained Mo-Co_3O_4-CNTc composites can be observed from the SEM images (Fig. 2a-b). Compared with the Mo-Co_3O_4 electrode materials (Fig. S3), the Mo-Co_3O_4-CNTc composites are composed of intertwisted and crinkly nanosheets to form hierarchically porous structures. Meanwhile, the CNTs were uniformly entangled and inserted into the Mo-Co_3O_4 nanosheets as express electron transport channels (Fig. S4). The detailed morphology of the hierarchically porous structures can be identified by TEM (Fig. 2c-f). The cross-linked and doped CNTs were combined with the Mo-Co_3O_4 nanosheets to form an interconnected electric network to facilitate the transfer of electrons. Notably, the interlaced ultrathin nanosheets reveal a thickness of 2–4 nm and substantial mesoporous scale holes, as shown in Fig. 2d. Meanwhile, the hierarchical mesoporous structures of Mo-Co_3O_4 nanosheets, combined with CNTs as an electric network, are beneficial for the rapid electrolyte ion diffusion and fast electrons transport with low resistance. Moreover, the nitrogen adsorption–desorption analysis (as Langmuir type IV, Fig. S5) [26, 53] indicated a BET surface area of 168.73 m^2 g^{-1}, BJH pore size distribution of ~3.9 nm, and pore volume 0.55 mL g^{-1}, respectively. Accordingly, the HRTEM image shown in Fig. 2f (inset) presents lattice spaces of 0.28, 0.23, and 0.20 nm, corresponding to the (220), (222), and (400) planes of Mo-Co_3O_4, indicating high crystallinity and the polycrystalline nature of the Mo-Co_3O_4 nanoparticles. Meanwhile, a lattice space of 0.34 nm was detected from the (002) plane of the CNTs in the Mo-Co_3O_4-CNTc composites. Additionally, the EDS pattern (inset Fig. 2d) shows the

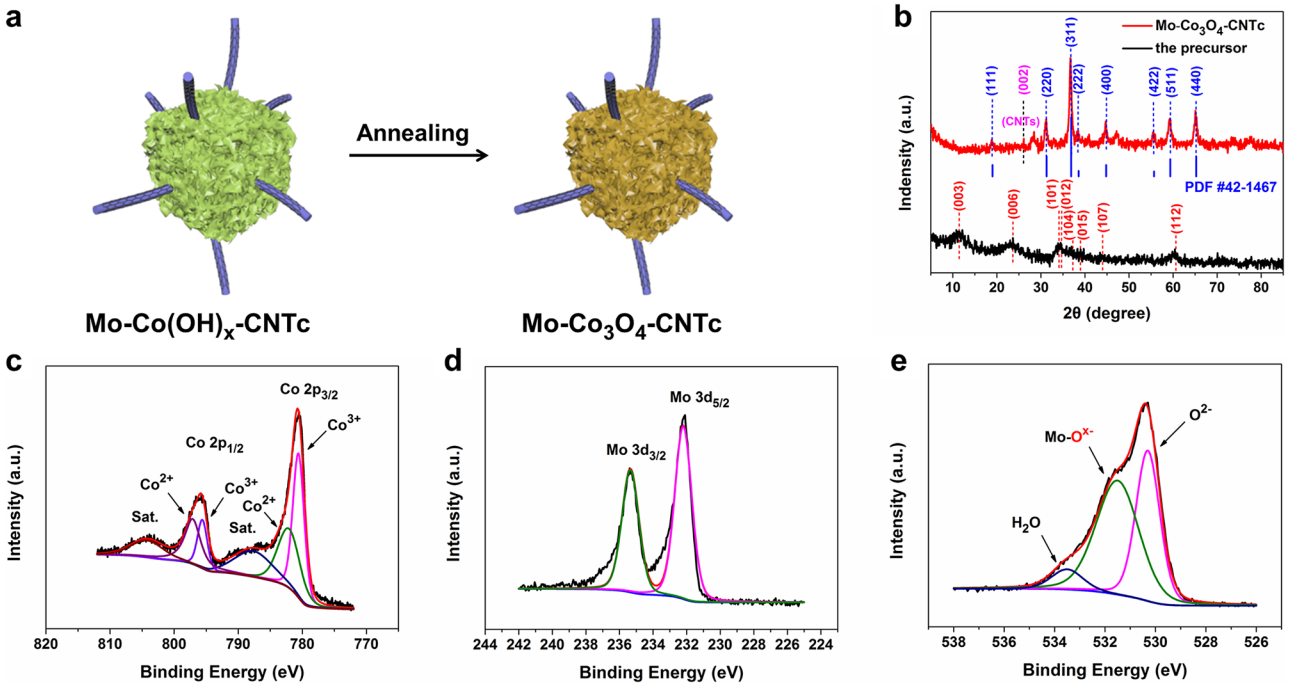

Fig. 1 **a** The schematic illustration of hierarchical porous Mo-Co_3O_4-CNTc composites. **b** XRD patterns. **c**–**e** The Co 2p, Mo 3d, and O 1 s spectra of Mo-Co_3O_4-CNTc

presence of Co, Mo, O, and C, thus further indicating the successful preparation of Mo-Co_3O_4-CNTc composites. The elemental mapping shows that these elements are distributed homogeneously on the entire Mo-Co_3O_4 nanosheets, as shown in Fig. 2g-k, which is consistent with the XPS results.

The electrochemical performance of the as-prepared Mo-Co_3O_4-CNTc composites was systematically evaluated in the three-electrode configuration. Compared with the pure Mo-Co_3O_4 electrode materials, the Mo-Co_3O_4-CNTc composites exhibited superior electrochemical properties, as demonstrated by the CV curves at 50 mV s^{-1} (Fig. 3a), GCD curves at 0.5 A g^{-1} (Fig. 3b), and average capacity (four samples) at various current densities (Fig. 3c). Moreover, the pure Co_3O_4 (as 107.3 mAh g^{-1} at 0.5 A g^{-1}) and a series of Mo-Co_3O_4 electrode materials with different Mo-Co molar ratios of 1:10, 5:10, and 10:10 were evaluated for comparison (Fig. 3d), indicating the superior electrochemical properties obtained at 1:10 as 112.0 mAh g^{-1} at 0.5 A g^{-1}. The CV curves of the Mo-Co_3O_4-CNTc cathode materials are exhibited in Fig. 3e with obvious battery-type features at multiple scan rates from 0.5 to 50 mV s^{-1}. The oxidative peaks shift toward more positive values and reductive peaks shift toward more negative values with the increase in scan rates due to the polarization effect and more reversible redox reactions. Furthermore, Fig. 3f shows the log *i* and log *v* plots at peak current values, and the *b*-values were determined to be 0.775 and 0.845 (in the range of 0.5–1.0) by the Dunn method [54], according to Eq. (4). Consequently, the as-prepared Mo-Co_3O_4-CNTc cathode materials represent both battery-type and pseudocapacitive-type characteristics.

$$\log i = b\log v + \log a \tag{4}$$

The capacitive contribution for the total current at 1 mV s^{-1} is shown in Fig. 3g. The contribution ratio of the capacitive and diffusion-controlled capacity at various scan rates (Fig. 3h) can be calculated by the following equations [55, 56]:

$$I = I_{cap} + I_{diff} = av^b \tag{5}$$

wherein I_{cap} and I_{diff} are the surface capacitance-led and diffusion-controlled current densities, respectively. The capacitive-controlled processes are 46.7%, 49.9%, 53.3%, 55.8%, 59.5%, 65.5%, 72.2%, 79.3%, and 91.3% at 0.5, 1, 2, 3, 5, 10, 20, 30, and 50 mV s^{-1}, respectively. Additionally, the typical GCD profiles at various current densities deliver a remarkable specific capacity of 152.9 mAh g^{-1} at 0.5 A g^{-1} and 82.7 mAh g^{-1} at 40 A g^{-1}, reaching 54.1% capacity retention, as shown in Fig. 3i. Compared with pure Co_3O_4 and Mo-Co_3O_4 electrode materials, the rate performance of Mo-Co_3O_4-CNTc showed enhanced specific capacity at the lower current density of 0.5 A g^{-1} in the initial 5 cycles. Thus, the last 15 cycles indicate good structural stability, as shown in Fig. 3j. Furthermore, Fig. 3k shows that excellent cycling performance was obtained, with 80.3% capacity retention after over 4000 GCD cycles at 25 A g^{-1} and a high Coulombic efficiency of 99.6%. Additionally, the

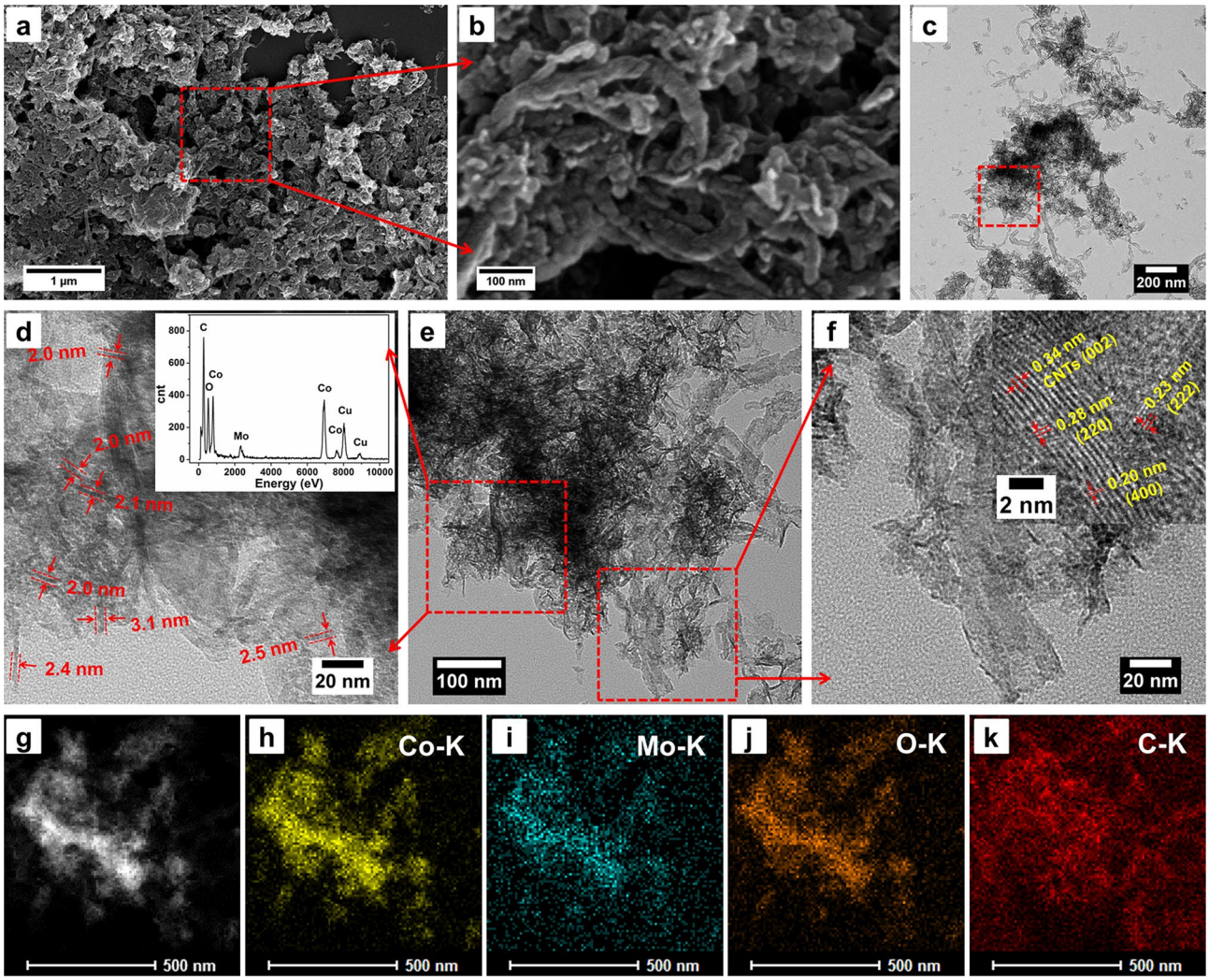

Fig. 2 The characterization of Mo-Co_3O_4-CNTc composites. **a**, **b** Different magnification SEM images. **c**–**f** Low- and high-magnification TEM images, EDS pattern, and HRTEM image (inset). **g**–**k** Co-K, Mo-K, O-K, and Cl-K

Nyquist plots (Fig. 3l) of Mo-Co_3O_4-CNTc show a lower electrochemical resistance (R_s) of around 0.43 Ω and a lower charge transfer resistance (R_{ct}) of 0.53 Ω, compared to both pure Co_3O_4 and Mo-Co_3O_4 electrode materials (Fig. S6). The superior properties of the Mo-Co_3O_4-CNTc composites can be attributed to the following factors: (i) the Mo-Co_3O_4, as a binary metal oxide, possesses higher electrical conductivity and electrochemical reactivity during the electrochemical processes due to the synergistic effect between the $Co^{2+}/Co^{3+}/Co^{4+}$ and Mo^{6+}/Mo^{4+} redox couples; (ii) the hierarchical porous structures provide open spaces for ion-buffering reservoirs, filled with electrolyte ions during the charge-discharge process, and substantial mesoporous structures in the ultrathin nanosheets exhibited short ion-diffusion channels from the external electrolyte to the interior of the Mo-Co_3O_4 nanosheets, thus leading to long cycling life and low internal resistance, respectively; and (iii) the Mo-Co_3O_4-CNTc composites with interpenetrating CNTs forming 3D conductive networks led to "express channels" through the hierarchical porous Mo-Co_3O_4 electrode materials to further synergistically improve the electron transport and electrochemical performance.

As illustrated in Fig. 4a, the MoCo-Zn batteries were assembled with the hierarchically porous Mo-Co_3O_4-CNTc composites as the advanced cathode materials and zinc metal as the anode, in the 6 M KOH aqueous electrolyte with 0.2 M zinc acetate. The CV curves of the MoCo-Zn batteries exhibited similar shapes and redox peaks, with the increasing scan rate from 0.5 to 50 mV s^{-1} (Fig. 4b). The *b* values of the MoCo-Zn batteries were calculated as 0.786 and 0.746 by the Dunn methods [54], as shown in Fig. 4c, thus revealing the coexistence of battery-type and pseudocapacitive-type characteristics. Moreover, the contribution ratio of capacitive and diffusion-controlled reactions is exhibited

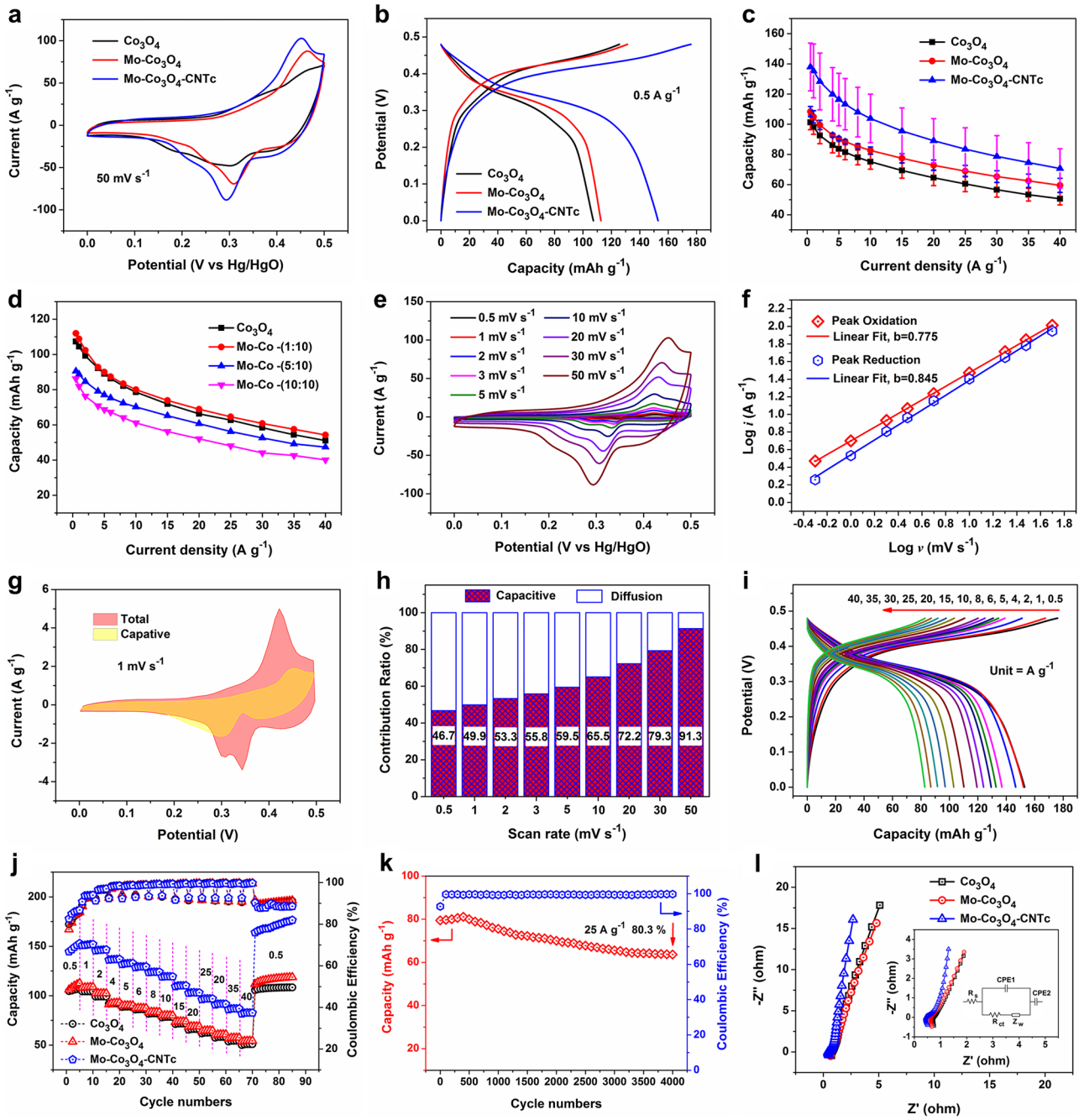

Fig. 3 The electrochemical properties of Co_3O_4, Mo-Co_3O_4, and Mo-Co_3O_4-CNTc for comparison: **a** CV curves, **b** GCD curves, **c** rate performance, and **d** rate performance with different Mo-Co molar ratios. The electrochemical properties of Mo-Co_3O_4-CNTc composites (with the Mo-Co molar ratio of 1:10): **e** CV curves, **f** *b* value, **g** capacitive contribution for the total current at 1 mV s^{-1}, **h** capacitive and diffusion-controlled proportions at various scan rates, **i** GCD curves, **j** rate performance, **k** cycling performance, and **l** Nyquist plots and equivalent circuit (inset)

in Fig. 4d as 48.0%, 51.5%, 53.8%, 55.3%, 56.6%, 57.6%, 59.4%, 61.1%, 65.3%, 69.0%, 75.1%, 81.6%, and 86.8% at various scan rates of 1, 2, 3, 4, 5, 6, 8, 10, 15, 20, 30, 40, and 50 mV s^{-1}, respectively. Furthermore, the GCD curves with an average discharge platform of around 1.68 V represent the voltage window of 1.93 V from 1 to 30 A g^{-1}, as shown in Fig. 4e, and deliver the specific capacity of 195.7 mAh g^{-1} at 0.5 A g^{-1} and 97.6 mAh g^{-1} at 30 A g^{-1} (with capacity utilization of 49.9%), respectively. The MoCo-Zn batteries display outstanding rate performance and Coulombic efficiency, as shown in Fig. 4f, thus demonstrating good structural stability. Meanwhile, the energy density and power

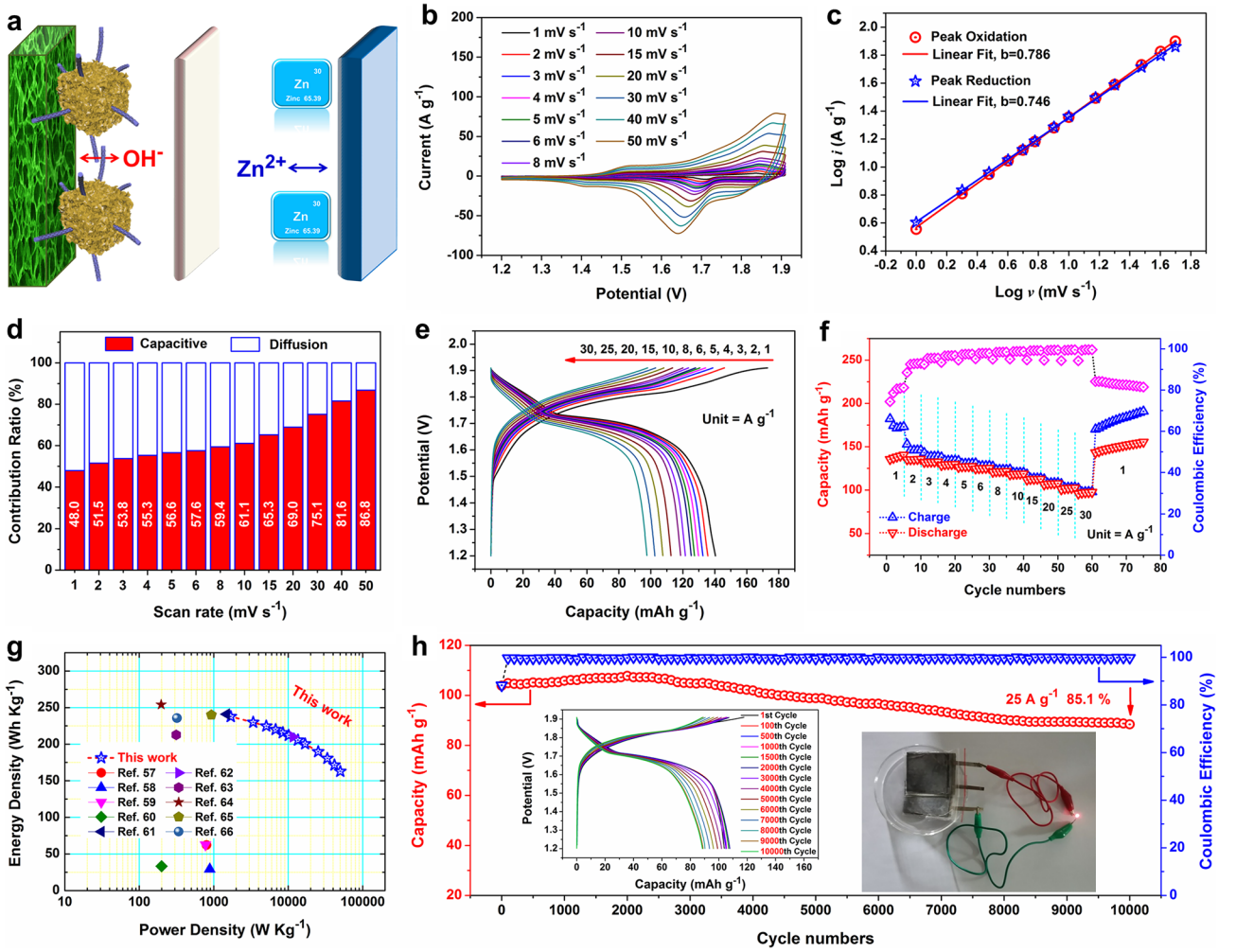

Fig. 4 **a** Schematic illustration of the MoCo-Zn batteries. Electrochemical performance of the batteries: **b** CV curves, **c** *b* value in CV curves, **d** capacitive and diffusion-controlled proportions at various scan rates, **e** GCD curves, **f** rate performance, **g** Ragone plots, and **h** cycling performance, the inset shows GCD curves at different cycles and the photographs of red-light emitting diodes (LEDs) lighted by MoCo-Zn batteries in series

density can be evaluated from the Ragone plots (Fig. 4g) as 237.6 Wh kg^{-1} at 1692.4 W kg^{-1} and 162.7 Wh kg^{-1} at 50,032.0 W kg^{-1}, respectively. Compared with the Mo-Co-based supercapacitors and other aqueous rechargeable ZIBs, the as-prepared MoCo-Zn batteries exhibited a superior energy density, such as $CoMoO_{4-x}$//AC 62.3 Wh kg^{-1} at 800 W kg^{-1} [57], $ZnCo_2O_4$@$CoMoO_4$//AC 29.24 Wh kg^{-1} at 884.57 W kg^{-1} [58], $CoMoO_4$@$Ni(OH)_2$//AC 62.5 Wh kg^{-1} at 776 W kg^{-1} [59], $NiMoO_4$/$CoMoO_4$//AC 33.1 Wh kg^{-1} at 199.6 W kg^{-1} [60], Zn//Co_3O_4 241 Wh kg^{-1} at 1487.7 W kg^{-1} [61], Zn//NiCo 210.1 Wh kg^{-1} at 11600 W kg^{-1} [62], Zn//core-shell Co_3O_4@δ-MnO_2/CC 212.8 Wh kg^{-1} at 313.3 W kg^{-1} [63], Zn//MnO_2 254 Wh kg^{-1} at 197 W kg^{-1} [64], Zn//P-MoO_{3-x}@Al_2O_3 240 Wh kg^{-1} at 931.3 W kg^{-1} [65], and Zn//$LiVPO_4F$-CNTs@PPy 235.6 Wh kg^{-1} at 320.8 W kg^{-1} [66]. The MoCo-Zn batteries exhibited excellent cycling performance, with 85.1% capacity retention over 10,000 cycles at 25 A g^{-1}, and there was no decay at the initial 2000 cycles (Fig. 4h). Meanwhile, the Mo-Co_3O_4-CNTc composites also possessed hierarchical porous structures with opened space functioning as "ion-buffering reservoirs" [67–69], which outperformed most aqueous rechargeable ZIBs. Furthermore, the Coulombic efficiency of the MoCo-Zn batteries was nearly 100%. The inset (Fig. 4h) displays GCD curves at different cycles from 1st to 10,000th, thus indicating the changes in the GCD curves during long-term cycling life, including capacity decay, electrode polarization, stabilization of Coulombic efficiency, and displacement of the discharge platform. Finally, the LEDs (2.2 V, 0.06 W) could be lit up by a series of MoCo-Zn devices, as demonstrated in Fig. 4h (inset image), verifying their potential for practical applications.

To further investigate the MoCo-Zn batteries, the summary of Zn^{2+} ion storage mechanism of Mo-Co_3O_4-CNTc was explored via ex situ XRD patterns, Raman spectra, and XPS measurements to characterize the structural evolution at certain voltages. Figure 5a represents the schematic illustration of the charge-discharge process with Zn^{2+} intercalation/de-intercalation. Figure 5b represents the different states in the charge-discharge process, labeled C0, C1, C2, C3, C4, D2, D1, and D0 (where C and D represent charge and discharge, respectively). As shown in ex situ XRD patterns (Fig. 5c), the diffraction peaks shift at around 2θ = 20°, corresponding to the (111) planes of Co_3O_4 after the intercalation/de-intercalation of Zn^{2+} during the charge-discharge process. Simultaneously, the new diffraction peaks appeared in the range of 11–13°, thus signifying a new layer of α-$Co(OH)_2$ on the surface of the C3, C4, D2, and D1 states. Moreover, the ex situ Raman spectra (Fig. 5d) show that the peaks shifted to a higher value at around 666 cm^{-1} in the states labeled C2, C3, C4, D2, and D1, according to the Zn^{2+} ingress/egress. Additionally, more detailed information of the chemical composition and states can be further investigated by ex-XPS measurements (Fig. S7). Compared with the state of C0 without the Zn 2p region, the Zn 2p spectrum (Fig. 5e) can be detected as the absorbed Zn^{2+} at Zn $2p_{3/2}$ at 1022.0 eV and Zn $2p_{1/2}$ at 1045.1 eV, and the intercalated Zn^{2+} at Zn $2p_{3/2}$ at 1021.4 eV and Zn $2p_{1/2}$ at 1044.5 eV [70]. Thus, during the discharge/charge process, the Zn^{2+} intercalation/de-intercalation can be further demonstrated, with the intensity of intercalated Zn^{2+} peaks increasing in the C1, C2, C3, and C4 states and decreasing of intercalated Zn^{2+} peaks in the D2, D1, and D0 states. Furthermore, the Mo 3d spectrum (Fig. 5f) of the Mo-Co_3O_4-CNTc cathode materials could be deconvoluted as Mo $3d_{5/2}$ and Mo $3d_{3/2}$, corresponding to Mo^{6+} at 232.2 eV, Mo^{4+} at 231.7 eV, Mo^{6+} at

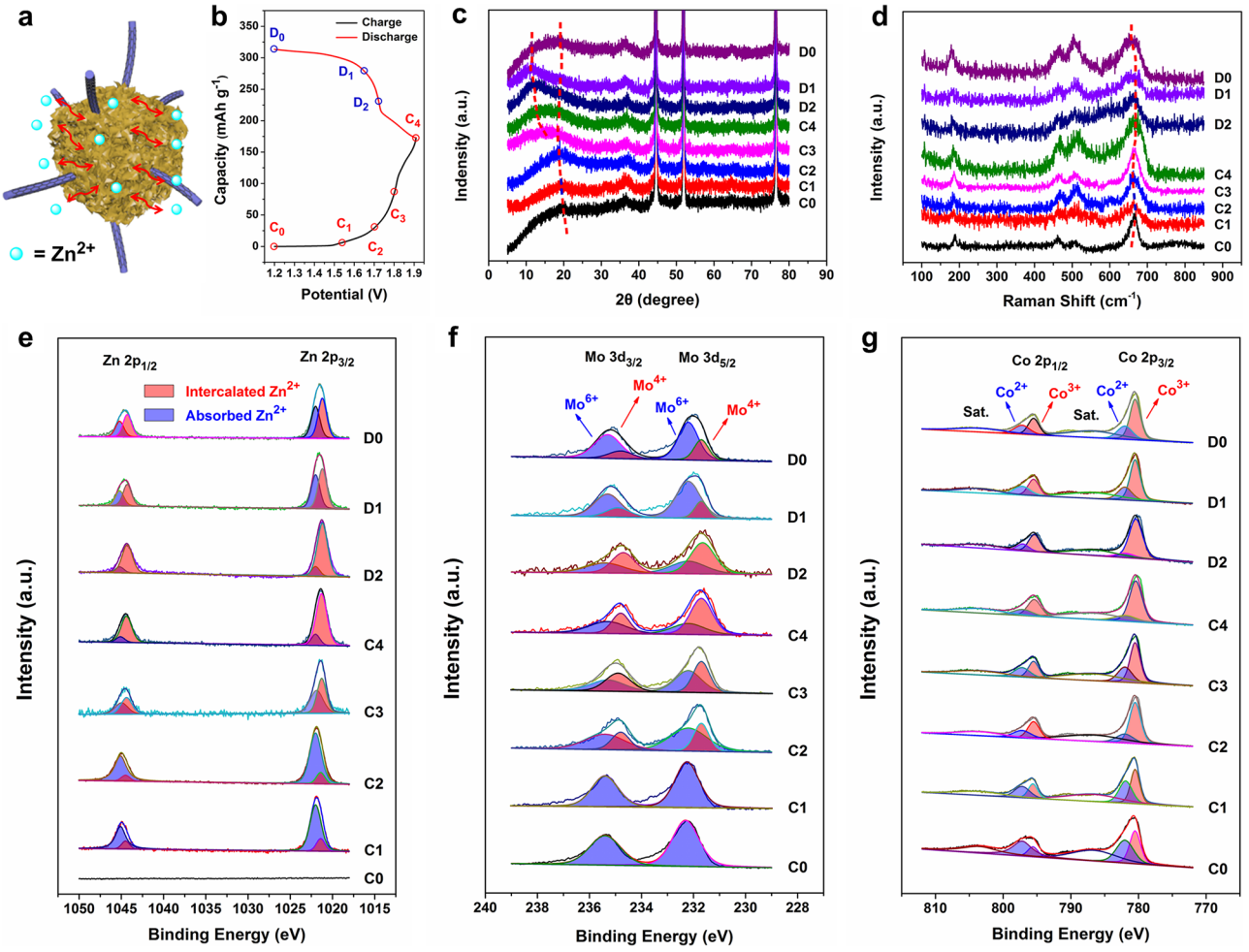

Fig. 5 **a** The schematic illustration of charge-discharge process of Mo-Co_3O_4-CNTc cathode materials. The characterization of different labeled states from C0 to D0 during the charge-discharge process: **b** GCD curve, **c** ex situ XRD patterns, **d** ex situ Raman spectra, **e**–**g** Zn 2p, Mo 3d, and Co 2p XPS spectra

235.3 eV, and Mo^{4+} at 234.9 eV, respectively, thus indicating the electrochemical reaction between the redox couple Mo^{6+}/Mo^{4+} during the charge-discharge processes. Similarly, the Co 2p spectra can be identified as the fitting peaks at 780.5 and 795.5 eV for Co^{3+}, and 782.0 and 797.0 eV for Co^{2+} [71, 72], respectively. Remarkably, the peaks of C3, C4, and D2 shift to lower binding energy due to more electrochemical oxidation of Co^{3+}, as shown in Fig. 5g. Furthermore, the C4 charge state of the Mo-Co_3O_4-CNTc composites maintained the hierarchically porous structures with nanosheets and the interpenetrating conductive networks of CNTc in the TEM images (Fig. 6a-c). Moreover, the EDS elemental pattern of the C4 charge state (Fig. 6d) indicates a homogeneous distribution of Zn, O, Co, Mo, and C, thus further indicating the Zn^{2+} intercalation/de-intercalation in the entire Mo-Co_3O_4-CNTc composite and a good agreement with XPS measurements.

To gain deep insight into the interaction between CNT and Mo-Co_3O_4, the structural and electronic properties of the Mo-Co_3O_4-CNT system were investigated by first-principles DFT calculations [73–75]. The optimized structures and corresponding plane-averaged electrostatic potentials of Co_3O_4, Mo-Co_3O_4, and Mo-Co_3O_4-CNT were calculated, as shown in Fig. 7a-c. No chemical bonds were formed at the interface, indicating a typical Van der Waals (vdW) interaction between CNT and Mo-Co_3O_4. Owing to the potential difference, an internal electric field formed at the interface, which is beneficial to charge transfer [76, 77]. In addition, the calculated work function of the Mo-Co_3O_4-CNT (4.6 eV) was lower than that of the Co_3O_4 surface (6.1 eV) and Mo-Co_3O_4 surface (5.4 eV). The smaller work function means less loss when electrons escape to the surface for electron emission. This suggests that the Mo-Co_3O_4-CNT composite is beneficial for achieving high electronic conductivity. The differences in charge density and plane-averaged charge density of Co_3O_4, Mo-Co_3O_4, and Mo-Co_3O_4-CNT are plotted in Fig. 7d-f. The positive (yellow region) and negative (cyan

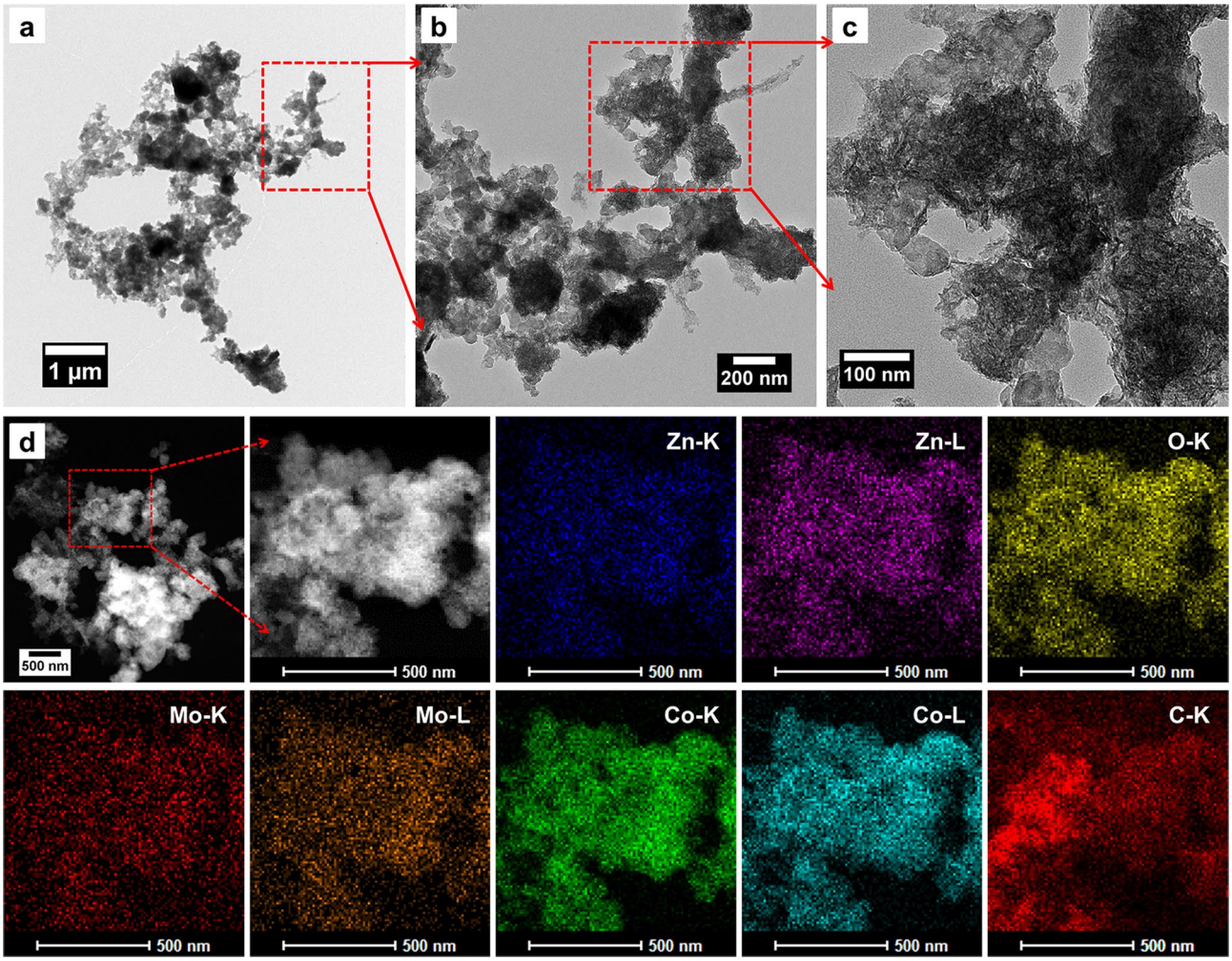

Fig. 6 The morphology of C4 charge state: **a**–**c** low- and high-magnification TEM images and **d** the EDS elemental mapping analysis of Zn, O, Mo, Co, and C

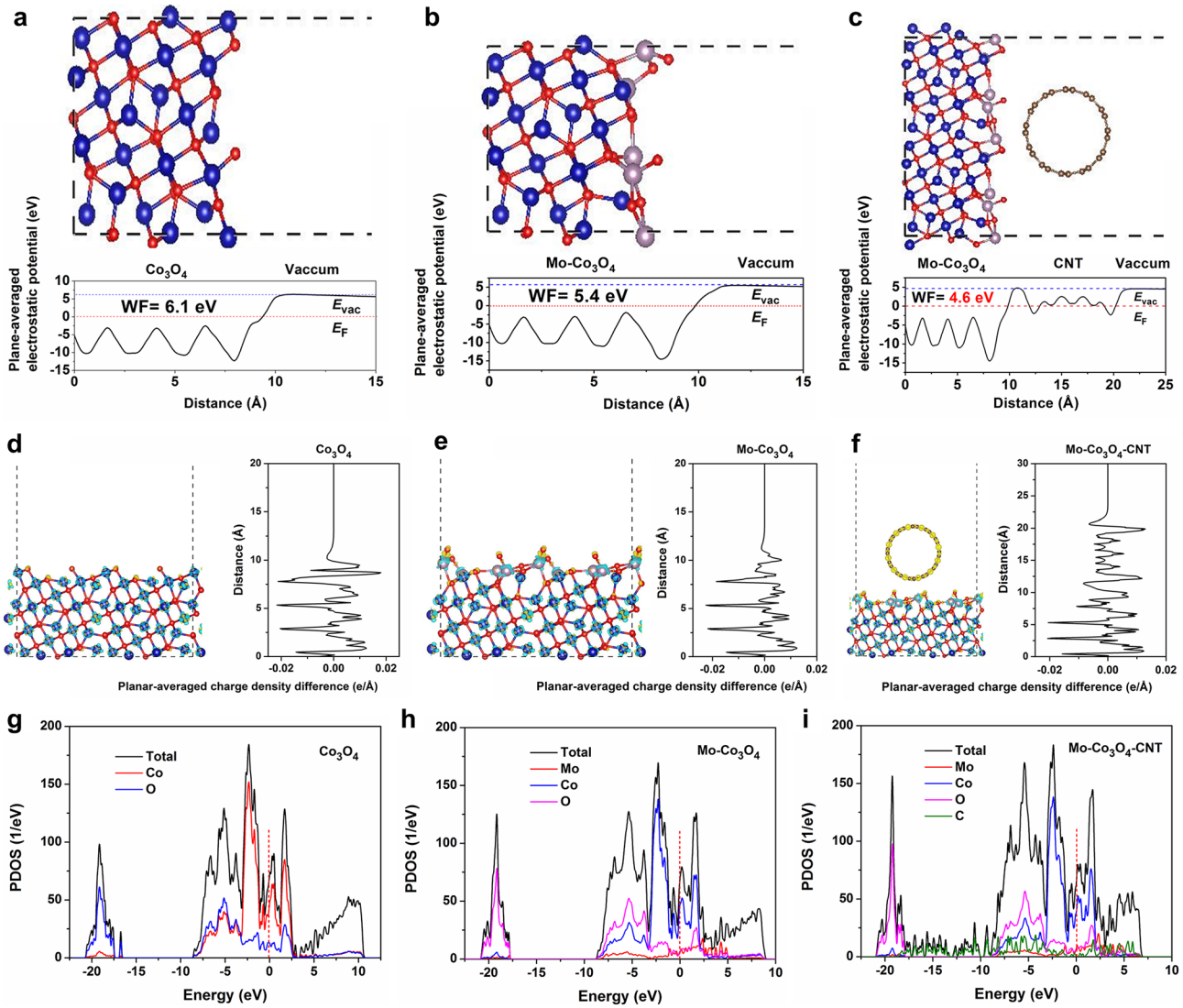

Fig. 7 Density-functional first-principles calculations of Co_3O_4, Mo-Co_3O_4, and Mo-Co_3O_4-CNT composites for comparison: **a–c** optimized structure and plane-averaged electrostatic potential, **d–f** calculated charge density difference, and plane-averaged charge density difference, **g–i** atom-projected density of states (DOS). Color scheme: Co, blue; Mo, purple; O, red; C, brown. TOC: The cathode materials of Mo-doped in hierarchical porous Mo-Co_3O_4-CNTc composites were fabricated for aqueous rechargeable zinc ions batteries with ultra-long cycle life

region) values indicate charge accumulation and depletion, respectively. The Bader charge analysis shows that 0.06 e^- per supercell was transferred from CNT to Mo-Co_3O_4. This indicates that Mo-Co_3O_4-CNT interfaces improve electron transport at the Mo-Co_3O_4 surface. To further study the interfacial contact properties, the atom-projected density of states (DOS) were analyzed, as shown in Fig. 7g-i. The increase in the density of states around the Fermi level resulted in increased conduction at elevated energies. CNT could alter the density of states and, therefore, alter the conductivity at the interface without damaging the significant characteristics of the Mo-Co_3O_4 surface [78]. This result is in good agreement with the EIS measurements.

4 Conclusions

In summary, we report the synthesis and investigation of hierarchical porous Mo-Co_3O_4-CNTc composites as cathode materials for aqueous rechargeable ZIBs. The interpenetrating CNTs act as "express channels," leading to 3D conductive networks that improve electronic conductivity. Experimental electrochemical data and first-principles DFT calculations demonstrated that hierarchical porous Mo-Co_3O_4-CNTc composites showed superior electrochemical properties compared to pure Mo-Co_3O_4 electrode materials. Furthermore, the assembled MoCo-Zn batteries exhibited a specific capacity of 195.7 mAh g^{-1} at 0.5 A g^{-1}, 237.6

Wh kg^{-1} at 1692.4 W kg^{-1}, and ultralong cycling performance, with a 85.1% capacity retention over 10,000 cycles. The Zn^{2+} ion storage mechanism in the Mo-Co_3O_4-CNTc cathode was further investigated to study the structural evolution at certain voltages. Therefore, in this study, we provide an innovative strategy for constructing the M'-doped metal oxide composites modified with carbon materials (M'-MO_x/carbon), by a typical sol-gel emulsion method to help develop next-generation aqueous rechargeable batteries for energy storage and conversion.

Supplementary Information The online version contains supplementary material available at https://doi.org/10.1007/s42114-023-00669-6.

Author contribution Changwei Lai carried out the experimental parts of materials synthesis and characterizations, and wrote the main manuscript text. Xiaoxiao Qu prepared Fig. 1a. Yao Guo wrote the part "2.6 Computational methods" and prepared Fig. 7. Miaomiao Li prepared some data curation. Haixiang Song and Kwan Lee contributed the writing-review and editing, and funding acquisition. All authors reviewed the manuscript.

Funding This work was supported by the Science and Technology Project of Henan Province (nos. 222102240103 and 192102210048); the Natural Science Foundation of Henan Province (no. 212300410099); the Basic Science Research Program through the National Research Foundation of Korea (NRF) funded by the Ministry of Education (NRF2020R1I1A3070962); and the Ph. D. Research Start-up Fund of Anyang Institute of Technology (no. BSJ2019033).

Declarations

Conflict of interest The authors declare no competing interests.

References

1. Pu LY, Zhang JX, Jiresse NKL, Gao YF, Zhou HJ, Naik N, Gao P, Guo ZH (2022) N-doped MXene derived from chitosan for the highly effective electrochemical properties as supercapacitor. Adv Compos Hybrid Mater 5:356–369
2. Ahmed FBM, Khalafallah D, Zhi MJ, Hong ZL (2022) Porous nanoframes of sulfurized NiAl layered double hydroxides and ternary bismuth cerium sulfide for supercapacitor electrodes. Adv Compos Hybrid Mater 5:2500–2514
3. Qu KQ, Sun Z, Shi C, Wang WC, Xiao LD, Tian JY, Huang ZH, Guo ZH (2021) Dual-acting cellulose nanocomposites filled with carbon nanotubes and zeolitic imidazolate framework-67 (ZIF-67)-derived polyhedral porous Co_3O_4 for symmetric supercapacitors. Adv Compos Hybrid Mater 4:670–683
4. Xiao LD, Qi HJ, Qu KQ, Shi C, Cheng Y, Sun Z, Yuan BN, Huang ZH, Pan D, Guo ZH (2021) Layer-by-layer assembled free-standing and flexible nanocellulose/porous Co_3O_4 polyhedron hybrid film as supercapacitor electrodes. Adv Compos Hybrid Mater 4:306–316
5. Ma YP, Xie XB, Yang WY, Yu ZP, Sun XQ, Zhang YP, Yang XY, Kimura H, Hou CX, Guo ZH, Du W (2021) Recent advances in transition metal oxides with different dimensions as electrodes for high-performance supercapacitors. Adv Compos Hybrid Mater 4:906–924
6. Liu L, Guo ZY, Yang J, Wang SY, He ZF, Wang C (2021) High ion selectivity Aquivion-based hybrid membranes for all vanadium redox flow battery. Adv Compos Hybrid Mater 4:451–458
7. Hou CX, Wang B, Murugadoss V, Vupputuri S, Chao YF, Guo ZH, Wang CY, Du W (2020) Recent advances in Co_3O_4 as anode materials for high-performance lithium-ion batteries. Eng Sci 11:19–30
8. Hou CX, Yang WY, Kimura H, Xie XB, Zhang XY, Sun XQ, Yu ZP, Yang XY, Zhang YP, Wang B, Xu BB, Sridhar D, Algadi H, Guo ZH, Du W (2023) Boosted lithium storage performance by local build-in electric field derived by oxygen vacancies in 3D holey N-doped carbon structure decorated with molybdenum dioxide. J Mater Sci Technol 142:185–195
9. Hou CX, Yang WY, Xie XB, Sun XQ, Wang J, Naik N, Pan D, Mai XM, Guo ZH, Dang F, Du W (2021) Agaric-like anodes of porous carbon decorated with MoO_2 nanoparticles for stable ultralong cycling lifespan and high-rate lithium/sodium storage. J Colloid Interface Sci 596:396–407
10. Dang CC, Mu Q, Xie XB, Sun XQ, Yang XY, Zhang YP, Maganti S, Huang MN, Jiang QL, Seok I, Du W, Hou CX (2022) Recent progress in cathode catalyst for nonaqueous lithium oxygen batteries: a review. Adv Compos Hybrid Mater 5:606–626
11. Zhai YJ, Yang WY, Xie XB, Sun XQ, Wang J, Yang XY, Naik N, Kimura H, Du W, Guo ZH, Hou CX (2022) Co_3O_4 nanoparticles dotted hierarchical-assembled carbon nanosheet frameworks catalysts with formation/decomposition mechanisms of Li_2O_2 for smart lithium-oxygen batteries. Inorg Chem Front 9:1115–1124
12. Liu HY, Xu T, Liang QD, Zhao QS, Zhao DW, Si CL (2022) Compressible cellulose nanofibrils/reduced graphene oxide composite carbon aerogel for solid-state supercapacitor. Adv Compos Hybrid Mater 5:1168–1179
13. Yang ZL, Han L, Fu XB, Wang YL, Huang HL, Xu M (2022) Double-safety flexible supercapacitor basing on zwitterionic hydrogel: over-heat alarm and flame-retardant electrolyte. Adv Compos Hybrid Mater 5:1876–1887
14. Zhao YL, Liu F, Zhu KJ, Maganti S, Zhao ZY, Bai PK (2022) Three-dimensional printing of the copper sulfate hybrid composites for supercapacitor electrodes with ultra-high areal and volumetric capacitances. Adv Compos Hybrid Mater 5:1537–1547
15. Yang WY, Peng DN, Kimura H, Zhang XY, Sun XQ, Pashameah RA, Alzahrani E, Wang B, Guo ZH, Du W, Hou CX (2022) Honeycomb-like nitrogen-doped porous carbon decorated with Co_3O_4 nanoparticles for superior electrochemical performance pseudo-capacitive lithium storage and supercapacitors. Adv Compos Hybrid Mater 5:3146–3157
16. Ma YP, Hou CX, Kimura H, Xie XB, Jiang HY, Sun XQ, Yang XY, Zhang YP, Du W (2023) Recent advances in the application of carbon-based electrode materials for high-performance zinc ion capacitors: a mini review. Adv Compos Hybrid Mater. https://doi.org/10.1007/s42114-023-00636-1
17. Maurya DK, Dhanusuraman R, Guo ZH, Angaiah S (2023) Na-ion conducting filler embedded 3D-electrospun nanofibrous hybrid solid polymer membrane electrolyte for high-performance Na-ion capacitor. Adv Compos Hybrid Mater. https://doi.org/10.1007/s42114-022-00604-1
18. Wang MM, Meng YH, Li K, Ahmad T, Chen N, Xu Y, Sun JF, Chuai MY, Zheng XH, Yuan Y, Shen CY, Zhang ZQ, Chen W (2021) High-performance Zn battery with transition metal ions co-regulated electrolytic MnO_2. eScience 1:178–185
19. Li TC, Fang DL, Zhang JT, Pam ME, Leong ZY, Yu JZ, Li XL, Yan D, Yang HY (2021) Recent progress in aqueous zinc-ion batteries: a deep insight into zinc metal anodes. J Mater Chem A 9:6013–6028
20. Wang MM, Meng YH, Li K, Ahmad T, Chen N, Xu Y, Sun JF, Chuai MY, Zheng XH, Yuan Y, Shen CY, Zhang ZQ, Chen W (2022) Toward dendrite-free and anti-corrosion Zn anodes by regulating a bismuth-based energizer. eScience 2:509–517
21. Li JW, McColl K, Lu XK, Sathasivam S, Dong HB, Kang LQ, Li ZN, Zhao SY, Kafizas AG, Wang R, Brett DJL, Shearing

PR, Corà F, He GJ, Carmalt CJ, Parkin IP (2020) Multi-scale investigations of δ-$Ni_{0.25}V_2O_5{\cdot}nH_2O$ cathode materials in aqueous zinc-ion batteries. Adv Energy Mater 10:2000058
22. Lu YZ, Wang J, Zeng SQ, Zhou LJ, Xu W, Zheng DZ, Liu J, Zeng YX, Lu XH (2019) An ultrathin defect-rich Co_3O_4 nanosheet cathode for high-energy and durable aqueous zinc ion batteries. J Mater Chem A 7:21678–21683
23. Lu YF, Zhang HJ, Liu HD, Nie ZT, Xu F, Zhao Y, Zhu JX, Huang W (2021) Electrolyte dynamics engineering for flexible fiber-shaped aqueous zinc-ion battery with ultralong stability. Nano Lett 21:9651–9660
24. Xie YL, Fei B, Cai DP, Chen QD, Cui ZX, Wang QT, Zhan HB (2020) Multicomponent hierarchical $NiCo_2O_4$@$CoMoO_4$@Co_3O_4 arrayed structures for high areal energy density aqueous NiCo//Zn batteries. Energy Storage Mater 31:27–35
25. Zhao JK, Wei DN, Zhang C, Shao Q, Murugadoss V, Guo ZH, Jiang QL, Yang XJ (2021) An overview of oxygen reduction electrocatalysts for rechargeable zinc-air batteries enabled by carbon and carbon composites. Eng Sci 15:1–19
26. Mu Q, Liu RL, Kimura H, Li JC, Jiang HY, Zhang XY, Yu ZP, Sun XQ, Algadi H, Guo ZH, Du W, Hou CX (2023) Supramolecular self-assembly synthesis of hemoglobin-like amorphous CoP@N, P-doped carbon composites enable ultralong stable cycling under high-current density for lithium-ion battery anodes. Adv Compos Hybrid Mater. https://doi.org/10.1007/s42114-022-00607-y
27. Idrees M, Liu LQ, Batool S, Luo HB, Liang J, Xu BB, Wang S, Kong J (2019) Cobalt-doping enhancing electrochemical performance of silicon/carbon nanocomposite as highly efficient anode materials in lithium-ion batteries. Eng Sci 6:64–76
28. Hu SQ, Zhang ZW, Wang ZT, Zeng KY, Cheng Y, Chen J, Zhang G (2018) Significant reduction in thermal conductivity of lithium cobalt oxide cathode upon charging: propagating and non-propagating thermal energy transport. ES Energy Environ 1:74–79
29. Gadwal MS, Kaur J, Shaikh SF, Lokhande PE, Mathe VL, Sartale SD, Pathan HM (2022) Investigations on the magnetic properties of patterned cobalt grown on a mechanically scratched copper substrate. ES Mater Manuf 18:1–9
30. Lai CW, Wang SH, Cheng LL, Wang YX, Fu L, Sun Y, Lin BP (2021) High-performance asymmetric supercapacitors of advanced double ion-buffering reservoirs based on battery-type hierarchical flower-like Co_3O_4-GC microspheres and 3D holey graphene aerogels. Electrochim Acta 365:137334
31. Lai CW, Guo Y, Zhao HH, Song HX, Qu XX, Huang MN, Hong SW, Lee K (2022) High-performance double "ion-buffering reservoirs" of asymmetric supercapacitors enabled by battery-type hierarchical porous sandwich-like Co_3O_4 and 3D graphene aerogels. Adv Compos Hybrid Mater 5:2557–2574
32. Shen YN, Li ZH, Cui Z, Zhang K, Zou RJ, Yang F, Xu KB (2020) Boosting the interface reaction activity and kinetics of cobalt molybdate by phosphating treatment for aqueous zinc-ion batteries with high energy density and long cycle life. J Mater Chem A 8:21044–21052
33. Lv YL, Zhu L, Xu HX, Yang L, Liu ZP, Cheng DJ, Cao XH, Yun J, Cao DP (2019) Core/shell template-derived Co, N-doped carbon bifunctional electrocatalysts for rechargeable Zn-air battery. Eng Sci 7:26–37
34. Li GY, Dang CC, Hou Y, Dang F, Fan YQ, Guo ZH (2020) Experimental and theoretical characteristic of single atom Co-N-C catalyst for Li-O_2 batteries. Eng Sci 10:85–94
35. Peng ZY, Jiang QL, Peng P, Li FF (2021) NH_3-activated fullerene derivative hierarchical microstructures to porous Fe_3O_4/N-C for oxygen reduction reaction and Zn-air battery. Eng Sci 14:27–38
36. Fu YX, Pei XY, Dai Y, Mo DC, Lyu SS (2019) Three-dimensional graphene-like carbon prepared from CO_2 as anode material for high-performance lithium-ion batteries. ES Energy Environ 4:66–73
37. Mohamed Z, Zhang GL, He B, Fan YQ (2022) Heterostructure necklace-like NiO-$NiCo_2O_4$ hybrid with superior catalytic capability as electrocatalyst for Li-O_2 batteries. Eng Sci 17:231–241
38. Meng LT, Hou CP, Hou J, Xie HD, Yue ZY, Lu H, Yang SL, Gong BL (2022) Preparation and performance of in situ carbon-coated silicon monoxide@C@carbon microspheres composite anode material for lithium-ion batteries. Eng Sci 20:134–143
39. Lai CW, Wang YX, Fu L, Song HX, Liu B, Pan D, Guo ZH, Seok I, Li KW, Zhang HR, Dong MY (2022) Aqueous flexible all-solid-state NiCo-Zn batteries with high capacity based on advanced ion-buffering reservoirs of $NiCo_2O_4$. Adv Compos Hybrid Mater 5:536–546
40. Wei TY, Chen CH, Chien HC, Lu SY, Hu CC (2010) A cost-effective supercapacitor material of ultrahigh specific capacitances: spinel nickel cobaltite aerogels from an epoxide-driven sol-gel process. Adv Mater 22:347–351
41. Xiong SS, Weng ST, Tang Y, Qian L, Xu YQ, Li XF, Lin HJ, Xu YC, Jiao Y, Chen JR (2021) Mo-doped Co_3O_4 ultrathin nanosheet arrays anchored on nickel foam as a bi-functional electrode for supercapacitor and overall water splitting. J Colloid Interf Sci 602:355–366
42. Kresse G, Furthmüller J (1996) Efficiency of ab-initio total energy calculations for metals and semiconductors using a plane-wave basis set. Comp Mater Sci 6:15–50
43. Torres E, Kaloni TP (2020) Projector augmented-wave pseudopotentials for uranium-based compounds. Comp Mater Sci 171:109237
44. Blöchl PE (1994) Projector augmented-wave method. Phys Rev B 50:17953–17979
45. Perdew JP, Burke K, Ernzerhof M (1996) Generalized gradient approximation made simple. Phys Rev Lett 77:3865–3868
46. Methfessel M, Paxton AT (1989) High-precision sampling for Brillouin-zone integration in metals. Phys Rev B 40:3616–3621
47. Guterding D, Jeschke HO (2018) An efficient GPU algorithm for tetrahedron-based Brillouin-zone integration. Comput Phys Commun 231:114–121
48. Grimme S (2006) Semiempirical GGA-type density functional constructed with a long-range dispersion correction. J Comput Chem 27:1787–1799
49. Himmetoglu B, Floris A, Gironcoli S, Cococcioni M (2014) Hubbard-corrected DFT energy functionals: the LDA+U description of correlated systems. Int J Quantum Chem 114:14–49
50. Lai CW, Sun Y, Zhang XQ, Yang H, Kang WW, Lin BP (2018) Advanced flower-like Co_3O_4 with ultrathin nanosheets and 3D rGO aerogels as double ion-buffering reservoirs for asymmetric supercapacitors. Electrochim Acta 271:379–387
51. Lai CW, Sun Y, Zhang XQ, Yang H, Lin BP (2018) High-performance double ion-buffering reservoirs of asymmetric supercapacitors based on flower-like Co_3O_4-G>N-PEGm microspheres and 3D rGO-CNT>N-PEGm aerogels. Nanoscale 10:17293–17303
52. Yu MQ, Jiang LX, Yang HG (2015) Ultrathin nanosheets constructed $CoMoO_4$ porous flower with high activity for electrocatalytic oxygen evolution. Chem Commun 51:14361–14364
53. Li FS, Li QY, Kimura H, Xie XB, Zhang XY, Wu NN, Sun XQ, Xu BB, Algadi H, Pashameah RA, Alanazi AK, Alzahrani E, Li HD, Du W, Guo ZH, Hou CX (2023) Morphology controllable urchin-shaped bimetallic nickel-cobalt oxide/carbon composites with enhanced electromagnetic wave absorption performance. J Mater Sci Technol 148:250–259
54. Kim HS, Cook JB, Lin H, Ko JS, Tolbert SH, Ozolins V, Dunn B (2017) Oxygen vacancies enhance pseudocapacitive charge storage properties of MoO_{3-x}. Nat Mater 16:454–460
55. Hou LR, Shi YY, Zhu SQ, Rehan M, Pang G, Zhang XG, Yuan CZ (2017) Hollow mesoporous hetero-$NiCo_2S_4$/Co_9S_8 submicro-spindles: unusual formation and excellent pseudocapacitance towards hybrid supercapacitors. J Mater Chem A 5:133–144

56. Zhang HY, Wang JC, Sun Y, Zhang XQ, Yang H, Lin BP (2021) Wire spherical-shaped Co-MOF electrode materials for high-performance all-solid-state flexible asymmetric supercapacitor device. J Alloys Compd 879:160423
57. Li PX, Ruan CH, Xu J, Xie YB (2020) Supercapacitive performance of $CoMoO_4$ with oxygen vacancy porous nanosheet. Electrochim Acta 330:135334
58. Meng YN, Yu DY, Teng YF, Liu XL, Liu XY (2020) A high-performance electrode based on the $ZnCo_2O_4$@$CoMoO_4$ core-shell nanosheet arrays on nickel foam and their application in battery-supercapacitor hybrid device. Electrochim Acta 347:136278
59. Wang XH, Rong F, Huang FF, He P, Yang Y, Tang JP, Que RH (2019) Facile synthesis of hierarchical $CoMoO_4$@$Ni(OH)_2$ core-shell nanotubes for bifunctional supercapacitors and oxygen electrocatalysts. J Alloys Compd 789:684–692
60. Yu B, Jiang GH, Xu WC, Cao C, Liu YK, Lei N, Evariste U, Ma PP (2019) Construction of $NiMoO_4$/$CoMoO_4$ nanorod arrays wrapped by Ni-Co-S nanosheets on carbon cloth as high performance electrode for supercapacitor. J Alloys Compd 799:415–424
61. Wang XW, Wang FX, Wang LY, Li MX, Wang YF, Chen BW, Zhu YS, Fu LJ, Zha LS, Zhang LX, Wu YP, Huang W (2016) An aqueous rechargeable Zn//Co_3O_4 battery with high energy density and good cycling behavior. Adv Mater 28:4904–4911
62. Wang H, Liu J, Wang JQ, Hu MM, Feng YP, Wang PP, Wang YY, Nie NY, Zhang JH, Chen H, Yuan QH, Wu JW, Huang Y (2019) Concentrated hydrogel electrolyte-enabled aqueous rechargeable NiCo//Zn battery working from -20 to 50 °C. ACS Appl Mater Interfaces 11:49–55
63. Wang NZ, Yang GC, Gan Y, Wan HZ, Chen X, Wang C, Tan QY, Ji J, Zhao XJ, Liu PC, Zhang J, Peng XN, Wang HB, Wang Y, Ma GK, Aken P, Wang H (2020) Contribution of cation addition to MnO_2 nanosheets on stable Co_3O_4 nanowires for aqueous zinc-ion battery. Front Chem 8:793
64. Zhang N, Cheng FY, Liu JX, Wang LB, Long XH, Liu XS, Li FJ, Chen J (2017) Rechargeable aqueous zinc-manganese dioxide batteries with high energy and power densities. Nat Commun 8:405
65. Liu Y, Wang J, Zeng YX, Liu J, Liu XQ, Lu XH (2020) Interfacial engineering coupled valence tuning of MoO_3 cathode for high-capacity and high-rate fiber-shaped zinc-ion batteries. Small 16:1907458
66. Liu ZX, Yang Q, Wang DH, Liang GJ, Zhu YH, Mo FN, Huang ZD, Li XL, Ma LT, Tang TC, Lu ZG, Zhi CY (2019) A flexible solid-state aqueous zinc hybrid battery with flat and high-voltage discharge plateau. Adv Energy Mater 9:1902473
67. Lai CW, Cheng LL, Sun Y, Lee K, Lin BP (2021) Alkaline aqueous rechargeable Ni-Fe batteries with high-performance based on flower-like hierarchical $NiCo_2O_4$ microspheres and vines-grapes-like Fe_3O_4-NGC composites. Appl Surf Sci 563:150411
68. Lai CW, Qu XX, Zhao HH, Hong SW, Lee K (2022) Improved performance in asymmetric supercapacitors utilized by dual ion-buffering reservoirs based on honeycomb-structured $NiCo_2O_4$ and 3D rGO-PPy aerogels. Appl Surf Sci 586:152847
69. Lai CW, Lee K (2022) Double ion-buffering reservoirs of advanced NiCo//G-PANI asymmetric supercapacitors with high performance. J Alloys Compd 907:164490
70. Tang W, Lan BX, Tang C, An QY, Chen LN, Zhang WW, Zuo CL, Dong SJ, Luo P (2020) Urchin-like spinel MgV_2O_4 as a cathode material for aqueous zinc-ion battery. ACS Sustain Chem Eng 8:3681–3688
71. Lai CW, Sun Y, Zhang XQ, Yang H, Lin BP (2018) Gradual "OH^--incursion" outside-inside strategy in construction of 3D flower-like Co_3O_4-CNT>N-PEGm hierarchical microspheres for supercapacitors. Mater Today Energy 9:27–38
72. Lai CW, Sun Y, Lin BP (2019) Synthesis of sandwich-like porous nanostructure of Co_3O_4-rGO for flexible all-solid-state high-performance asymmetric supercapacitors. Mater Today Energy 13:342–352
73. Guo Y, Xue YB, Li CB, Li XC (2019) Electronic properties of the graphdiyne/$CH_3NH_3PbI_3$ interface: a first-principles study. Phy Status Solidi-R 14:1900544
74. Guo Y, Xue YB, Xu LQ (2021) Interfacial interactions and properties of lead oxysalts passivated $MAPbI_3$ perovskites from first-principles calculations. Comp Mater Sci 187:110081
75. Guo Y, Xue YB, Xu LQ (2021) Interfacial interactions and enhanced optoelectronic properties of GaN/perovskite heterostructures: insight from first-principles calculations. J Mater Sci 56:11352–11363
76. Hussain T, Singh D, Gupta SK, Karton A, Sonvane Y, Ahuja R (2019) Efficient and selective sensing of nitrogen containing gases by Si_2BN nanosheets under pristine and pre-oxidized conditions. Appl Surf Sci 469:775–780
77. Wang SS, Bu KJ, Wang D, Zheng C, Che XL, Han Z, Huang FQ (2021) Synthesis, crystal and electronic structure of a new ternary parkerite selenide $Pt_3Pb_2Se_2$. J Alloys Compd 853:157092
78. Barnett CJ, McCormack JE, Deemer EM, Evans CR, Evans JE, White AO, Dunstan PR, Chianelli RR, Cobley RJ, Barron AR (2020) Enhancement of multiwalled carbon nanotubes' electrical conductivity using metal nanoscale copper contacts and its implications for carbon nanotube-enhanced copper conductivity. J Phys Chem C 124:18777–18783

Publisher's Note Springer Nature remains neutral with regard to jurisdictional claims in published maps and institutional affiliations.

Springer Nature or its licensor (e.g. a society or other partner) holds exclusive rights to this article under a publishing agreement with the author(s) or other rightsholder(s); author self-archiving of the accepted manuscript version of this article is solely governed by the terms of such publishing agreement and applicable law.